ORIGINAL

A mixed convection in a reciprocating Π shape channel with opposite direction of gravity and inlet cooling fluids

Wu-Shung Fu · Sin-Hong Lian · Yu-Chih Lai

Abstract A numerical study is executed to investigate heat transfer mechanisms of a reciprocating channel cooled by fluids. The problem of the reciprocating piston is a moving boundary problem, and the Finite Element Method and arbitrary Largragian–Eulerian Kinematics method are then utilized. Due to the high temperature of the channel, a mixed convection is taken into consideration for simulating a more realistic situation. Directions of inlet cooling fluids and gravity are opposite. Concerning important parameters of the Reynolds number and Grashof number, reciprocating frequency and amplitude are examined. Thermal stratification layers which are found firmly on the top surface are deeply dependent on the magnitude of Gr/Re^2 ratio which directly affects the heat transfer mechanisms.

List of symbols

f_c	reciprocating frequency of the piston (s^{-1})
F_c	dimensionless reciprocating frequency of the piston
h_0	dimensional height of the piston (m)
Gr	Grashof number
h_1	dimensional height of the inlet channel and outlet channel (m)
l_c	reciprocating amplitude of the piston (m)
L_c	dimensionless reciprocating amplitude of the piston
$\dot{m}$	mass flow rate (kg s^{-1})
$\dot{M}$	dimensionless mass flow rate ($\dot{M} = \dot{m}/\rho_0 v_0 w \cdot 1$)
Nu_X	local Nusselt number
$\overline{Nu_X}$	average Nusselt number on the heat surface
$\overline{Nu}_C$	time-average Nusselt number per cycle
p	dimensional pressure (N m^{-2})
p_∞	reference pressure (N m^{-2})
P	dimensionless pressure
Pr	Prandtl number
Re	Reynolds number
t	dimensional time (s)
T	dimensional temperature (K)
T_0	dimensional temperature of the inlet fluid (K)
T_h	dimensional temperature of the heat surface (K)
u, v	dimensional velocities of in x and y directions (m s^{-1})
U, V	dimensionless velocities of in X and Y directions
v_0	dimensional velocities of the inlet fluid (m s^{-1})
V_0	dimensionless velocities of the inlet fluid
v_c	dimensional reciprocating velocity of the piston (m s^{-1})
V_c	dimensionless reciprocating velocity of the piston
v_m	dimensional maximum reciprocating velocity of the piston (m s^{-1})
V_m	dimensionless maximum reciprocating velocity of the piston
$\hat{v}$	dimensional mesh velocity in y-direction (m s^{-1})
$\hat{V}$	dimensionless mesh velocity in y-direction
w_0	dimensional width of the piston (m)
w	dimensional width of the channel (m)
W	dimensionless width of the channel
x, y	dimensional Cartesian coordinates (m)
X, Y	dimensionless Cartesian coordinates

Greek letters

α	thermal diffusivity (m^2 s^{-1})
Φ	computational variables
λ	penalty parameter

W.-S. Fu (✉) · S.-H. Lian · Y.-C. Lai
Department of Mechanical Engineering, National Chiao Tung University, 1001 Ta Hsueh Road, Hsinchu 30010, Taiwan, ROC
e-mail: wsfu@mail.nctu.edu.tw

v kinematics viscosity (m^2 s^{-1})

η_0 total length of the moving mesh region

η_1 length counted from the bottom of the moving mesh region

θ dimensionless temperature

ρ density (kg m^{-3})

τ dimensionless time

τ_p dimensionless time of one oscillating cycle

Ψ dimensionless stream function

Others

| | absolute value

1 Introduction

Protecting a piston from heat damage could effectively enhance the thermal efficiency of the heat engine and economize the usage of energy [1]. Lots of studies have been conducted to investigate similar objects recently.

Phenomena induced by a reciprocating straight channel which is somewhat similar to a reciprocating piston are interesting and have been widely investigated in the past. Grassma and Tuma [2] indicated that the mass transfer could achieve a level of about 2.5 times of the stationary case. Patera and Mikic [3] showed that the above enhancement might result from flows mixing due to hydrodynamic instability induced by pulsating flows. The results of Kim et al. [4] were that the pulsating amplitude affected heat transfer significantly and a heat transfer impediment relative to the nonpulsating situation might occur in the thermally developing flow region. Nishimura [5–8] utilized a sinusoidal wavy-walled channel replacing a smooth duct to investigate heat transfer enhancement by pulsating and oscillatory flows numerically and experimentally. The results indicated that the higher heat transfer rates appeared as Reynolds numbers rose, and the flow patterns which affected heat transfer rates were directly influenced by the frequency of oscillation remarkably. Chiu and Kuo [9] investigated turbulent heat transfer and predicted wall heat flux in a reciprocating engine by using an algebraic grid generation technique. The results showed that increasing the curvature of the cylinder head would increase the strength of induced squish flow and wall heat flux. Chang and Su [10] conducted an experimental work to investigate the influence of reciprocating motion on heat transfer inside a ribbed enclosure and showed that at the highest reciprocating speed, the heat transfer was enhanced about 145% of the equivalent stationary case. Chang and Su [1] modified the experiment and gained the results which at a pulsating number of 10.5, the time average Nusselt number could reach about 165% of the stationary one. Cheng and Hung [11] developed a solution method for predicting unsteady flow and thermal fields in a reciprocating piston–cylinder assembly. The results showed that the two-stage pressure correction procedure could be readily incorporated into existing numerical techniques to yield reasonably accurate results. Sert and Beskok [12] studied oscillatory flow forced convection in micro heat spreaders numerically. The results showed that a fluid with low viscosity, low density, and high thermal conductivity was desired in coolant selection. Khaled and Vafai [13] considered the influence of fluids inertia and the effects of the presence of a magnetic field normal to the direction of the flow of an electrically conducting fluid on flow and heat transfer inside a nonisothermal and incompressible thin film undergoing oscillatory squeezing. It was found that the increment of the squeezing Reynolds number caused the flow instability to increase. Oppositely, the increment of the Hartmann number would lead the flow instability to decrease. The Nusselt number would be affected by the increasing squeezing Reynolds number. Afterward, Chang et al. [14] set an anti-gravity open thermosiphon system which was a more realistic model of a piston cooling system than the ones proposed before to study the heat transfer of a piston under the conditions in which cooling fluids flow through the piston channel. Effects of inertia, pulsating and buoyancy forces were taken into consideration and a correlation formula which was consistent with the heat transfer physics expressed with dimensionless temperature was proposed. Recently, Fu et al. [15] assumed a Π shape channel as a piston to study a forced convection in the piston cooling system. The channel could move upward and downward periodically. The different parameters of the Reynolds number, amplitude and frequency were examined in detail.

However, the mechanisms of heat transfer taken into consideration in the stated literature were forced convection exclusively. The temperature of the piston is very high, and so consideration of natural convection effect should be added for a more realistic simulation. Usually, when a problem of mixed convection is investigated, a relationship between the directions of inlet cooling fluids and gravity should be examined at first. The physical model used in this study is a Π shape channel with a heat surface installed on the horizontal top surface of the Π shape channel. In such a situation, the directions of gravity and the inlet cooling fluids are downward and upward, respectively. In accordance with the direction of gravity, the heat surface which causes the densities of the neighboring fluids to be light is in the upper region and a stable thermal stratification layer is easily formed on the heat surface. The phenomena of the thermal stratification layer disturbed by the impingement of inlet cooling fluids become interesting problems and are valuably investigated.

Therefore, the aim of this study is to investigate heat transfer mechanisms of a reciprocating Π shape channel with opposite direction of gravity and inlet cooling fluids. Important parameters of Gr/Re^2, F_c, L_c are taken into consideration in detail. The processes of the thermal stratification layers disturbed by the impingement of inlet cooling fluids are examined clearly. The results show that the phenomena of heat transfer deeply depend on the dominance of the magnitude of Gr/Re^2 ratio.

2 Physical model

A physical model of two-dimensional Π shape channel simulating a piston used in this study is shown in Fig. 1. The total width and length of the channel are w_0 and h_0, respectively, and the channel width is w. The horizontal channel is the region surrounded by $\overline{BO'FGP'C}$. The top surface $\overline{BC}$ is a heat surface and at a constant temperature T_H, and the heat surface is cooled by inlet cooling fluids of which the temperature and velocity are T_0 and v_0, respectively. The inlet cooling fluids flow into the left vertical channel. The direction of gravity $\vec{g}$ is opposite to that of the inlet fluid velocity. Other surfaces of the channel are insulated. A part of the channel circled by $\overline{M'BCN'G'GFF'}$ is called a reciprocating channel and can move upwards and downwards reciprocally. The original length between $\overline{OP}$ and $\overline{MN}$ is w and can elongate to the maximum length of $2w$. The adjustable length w is utilized to simulate the

Fig. 1 Physical model of Π shape channel

moving distance of the reciprocating motion of the piston. Therefore, computation grids in this region are flexible. During the reciprocal motion of the channel, the $\overline{MN}$ is fixed and $\overline{OP}$ moves upwards with speed v_c, which causes the original region of the channel to be enlarged, and the maximum moving distance is w. Afterward, the $\overline{OP}$ moves downwards with the same speed v_c and returns to the original position. The mesh velocities of the computational grids inside the horizontal channel are equal to that of $\overline{OP}$. The length h_1 of the right channel is long enough for satisfying the convergent conditions of the temperature and velocity at the channel exit. The reciprocating velocity of channel is v_c, and can be expressed in terms of $v_c = v_m \sin (2\pi f_c t)$, where v_m is the maximum reciprocating velocity of the channel and equal to $2\pi f_c l_c$. When the channel moves reciprocally which affects the behaviors of the cooling fluid transiently, the motions of the cooling fluid become time-dependent which can be classified as a kind of moving boundary problem. As a result, the ALE method is properly employed to analyze this study.

For facilitating the analysis, the following assumptions are made.

(1) The fluid is air and the flow field is two-dimensional, incompressible and laminar.
(2) Except the density of the fluid, other properties of the fluid are assumed to be constant, and Boussinesq assumption is adopted.
(3) The no-slip condition is held on all the boundaries. Thus, the fluid velocities on the moving boundaries are equal to the moving velocities of the boundaries.

Based upon the characteristics scales of w, v_0, ρv_0^2, and T_0, the dimensionless variables are defined as follows:

$$
\begin{aligned}
&X = \frac{x}{w}, \quad Y = \frac{y}{w}, \quad U = \frac{u}{v_0}, \quad V = \frac{v}{v_0}, \quad \hat{V} = \frac{\hat{v}}{v_0} \\
&V_m = \frac{v_m}{v_0}, \quad V_c = \frac{v_c}{v_0}, \quad F_c = \frac{f_c w}{v_0}, \quad P = \frac{p - p_\infty}{\rho v_0^2} \\
&\tau = \frac{t v_0}{w}, \quad \theta = \frac{T - T_0}{T_h - T_0}, \quad Re = \frac{v_0 w}{v}, \quad Pr = \frac{v}{\alpha} \\
&Gr = \frac{g\beta(T_h - T_0)w^3}{v^2}, \quad V_c = V_m \sin(2\pi F_c \tau)
\end{aligned}
\tag{1}
$$

where $\hat{v}$ is defined as the mesh velocity, f_c, v_m, v_c are the reciprocating frequency, the maximum reciprocating velocity, and the instant reciprocating velocity of the piston, respectively.

According to the above assumptions and dimensionless variables, the dimensionless ALE governing equations are expressed as the following equations:

Continuity equation

$$
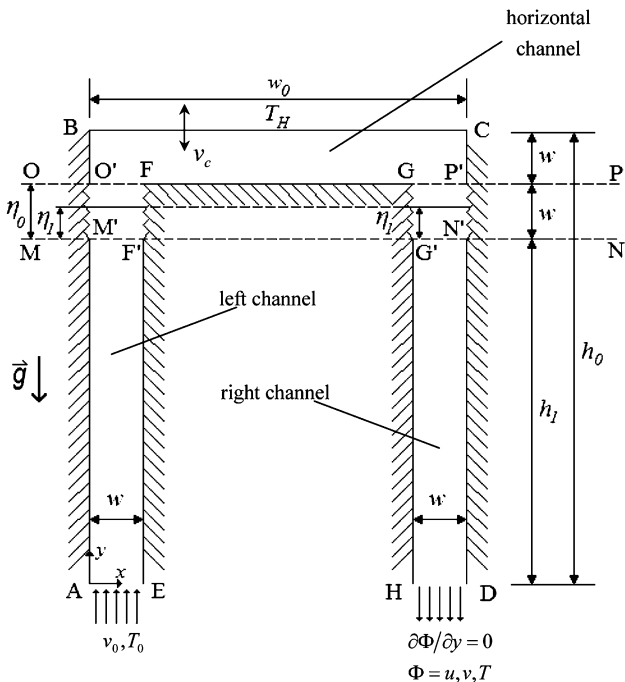\frac{\partial U}{\partial X} + \frac{\partial V}{\partial Y} = 0
\tag{2}
$$

Momentum equation

$$\frac{\partial U}{\partial \tau} + U\frac{\partial U}{\partial X} + (V - \hat{V})\frac{\partial U}{\partial Y} = -\frac{\partial P}{\partial X} + \frac{1}{Re}\left(\frac{\partial^2 U}{\partial X^2} + \frac{\partial^2 U}{\partial Y^2}\right) \tag{3}$$

$$\frac{\partial V}{\partial \tau} + U\frac{\partial V}{\partial X} + (V - \hat{V})\frac{\partial V}{\partial Y}$$
$$= -\frac{\partial P}{\partial Y} + \frac{1}{Re}\left(\frac{\partial^2 V}{\partial X^2} + \frac{\partial^2 V}{\partial Y^2}\right) + \frac{Gr}{Re^2}\theta \tag{4}$$

Energy equation

$$\frac{\partial \theta}{\partial \tau} + U\frac{\partial \theta}{\partial X} + (V - \hat{V})\frac{\partial \theta}{\partial Y} = \frac{1}{Re\,Pr}\left(\frac{\partial^2 \theta}{\partial X^2} + \frac{\partial^2 \theta}{\partial Y^2}\right) \tag{5}$$

In this study, the horizontal channel moves only vertically, therefore, the horizontal mesh velocity does not exist in the above governing equations. According to ALE method, the mesh velocity $\hat{V}$ is linearly distributed in the region between $\overline{MN}$(fixed) and $\overline{OP}$(movable). In the other regions, the mesh velocities are equal to 0.

Steady states of flow and thermal fields are used as initial conditions before the movement of the horizontal channel. The boundary conditions are as follows:

On the inlet surface $\overline{AE}$

$$U = 0, \quad V = 1, \quad \theta = 0 \tag{6}$$

On the outlet surface $\overline{HD}$

$$\frac{\partial U}{\partial Y} = 0, \quad \frac{\partial V}{\partial Y} = 0, \quad \frac{\partial \theta}{\partial Y} = 0 \tag{7}$$

On the walls $\overline{AM'}$, $\overline{EF'}$, $\overline{HG'}$, and $\overline{DN'}$

$$U = 0, \quad V = 0, \quad \frac{\partial \theta}{\partial X} = 0 \tag{8}$$

On the walls $\overline{M'O'}$, $\overline{F'F}$, $\overline{G'G}$, and $\overline{N'P'}$

$$U = 0, \quad V = \begin{cases} 0 & \tau = 0 \\ V_{\eta_1} & \tau = 0 \end{cases}, \quad \frac{\partial \theta}{\partial X} = 0 \tag{9}$$

On the walls $\overline{O'B}$, and $\overline{P'C}$

$$U = 0, \quad V = \begin{cases} 0 & \tau = 0 \\ V_c & \tau > 0 \end{cases}, \quad \frac{\partial \theta}{\partial X} = 0 \tag{10}$$

On the wall $\overline{FG}$

$$U = 0, \quad V = \begin{cases} 0 & \tau = 0 \\ V_c & \tau > 0 \end{cases}, \quad \frac{\partial \theta}{\partial Y} = 0 \tag{11}$$

On the wall $\overline{BC}$

$$U = 0, \quad V = \begin{cases} 0 & \tau = 0 \\ V_c & \tau > 0 \end{cases}, \quad \theta = 1 \tag{12}$$

where V_{η_1} is the mesh velocity of the position η_1 and proportional to the distance between $\overline{MN}$ and $\overline{OP}$, and is defined as following equation:

$$V_{\eta_1} = \frac{\eta_1}{\eta_0} \cdot V_c \tag{13}$$

3 Numerical method

The governing equations and boundary conditions are solved by the Galerkin finite element formulation and a backward scheme is adopted to deal with the time terms of the governing equations. The pressure is eliminated from the governing equations by using the consistent penalty method [16]. The velocity and temperature terms are expressed as a quadrilateral element and eight-node quadratic Lagrangian interpolation utilized to simplify the non-linear terms in the momentum equations. The discretion processes of the governing equations are similar to the one used in Fu et al. [15]. Then, the governing equations 3, 4, and 5 can be expressed as the following matrix forms:

$$\sum_1^{n_e}\left([A]^{(e)} + [K]^{(e)} + \lambda[L]^{(e)}\right)\{q\}_{\tau+\Delta\tau}^{(e)} = \sum_1^{n_e}\{f\}^{(e)} \tag{14}$$

where

$$\left(\{q\}_{\tau+\Delta\tau}^{(e)}\right)^T = \langle U_1, U_2, \ldots, U_8, V_1, V_2, \ldots, V_8,.$$
$$\theta_1, \theta_2, \ldots, \theta_8\rangle_{\tau+\Delta\tau}^{m+1} \tag{15}$$

$[A]^{(e)}$ includes the (m)th iteration values of U, V and θ at time $\tau + \Delta\tau$; $[K]^{(e)}$ includes the shape function, $\hat{V}$, and time differential terms; $[L]^{(e)}$ includes the penalty function; $\{f\}^{(e)}$ includes the known values of U, V and θ at time τ and (m)th iteration values of U, V and θ at time $\tau + \Delta\tau$

In Eq. 14, Gaussian quadrature procedure is conveniently used to execute the numerical integration. The terms with the penalty parameter λ are integrated by 2×2 Gaussian quadrature, and the other terms are integrated by 3×3 Gaussian quadrature. The value of the penalty parameter λ used in this study is 10^6. The frontal method solver is used to solve Eq. 14.

A brief outline of the solution procedures are described as follows:

(1) The optimal mesh distribution and number of the elements and nodes are determined.
(2) The values of the U, V, and θ at the steady state are solved and those are regarded as the initial values in the transient state.
(3) The time step $\Delta\tau$ and the mesh velocity $\hat{V}$, of the computational meshes are determined.
(4) The coordinates of the nodes are updated and the determinant of the Jacobian transformation matrix are examined to ensure the one to one mapping to be satisfied during the Gaussian quadrature numerical integration.

(5) Equation 14 is solved, until the following criteria for convergence are satisfied:

$$\left| \frac{\Phi^{m+1} - \Phi^m}{\Phi^{m+1}} \right|_{\tau+\Delta\tau} < 10^{-3} \tag{16}$$

where $\Phi = U, V$ and θ.

(6) The next time step calculation is followed until periodic solutions are attained.

4 Results and discussion

The working fluid is air and $Pr = 0.7$. Combinations of main parameters are tabulated in Table 1. To obtain the optimal computational mesh, three different elements are used for mesh tests. Figure 2 shows distributions of local Nusselt numbers on the heat surface with three different elements under $Re = 500$, $Gr/Re^2 = 40$ situation. The local Nusselt number Nu_X of the heat surface at time τ, the average Nusselt number $\overline{Nu_X}$ of the heat surface at time τ, and the cyclical average Nusselt number $\overline{Nu}_c$ are calculated by the following equations, respectively.

$$Nu_X = -\frac{\partial\theta}{\partial Y} \tag{17}$$

$$\overline{Nu_X} = \frac{1}{w_0} \int\limits_{\overline{BC}} Nu_X \, dX \tag{18}$$

$$\overline{Nu_c} = \frac{1}{\tau_p} \int\limits_{\tau_p} \overline{Nu_X} \, d\tau \tag{19}$$

where τ_p is a cyclical time.

According to the results, the computational mesh with 13,176 elements which corresponds to 41,029 nodes is used through all analyses in this study.

Table 1 Computed parameter combinations

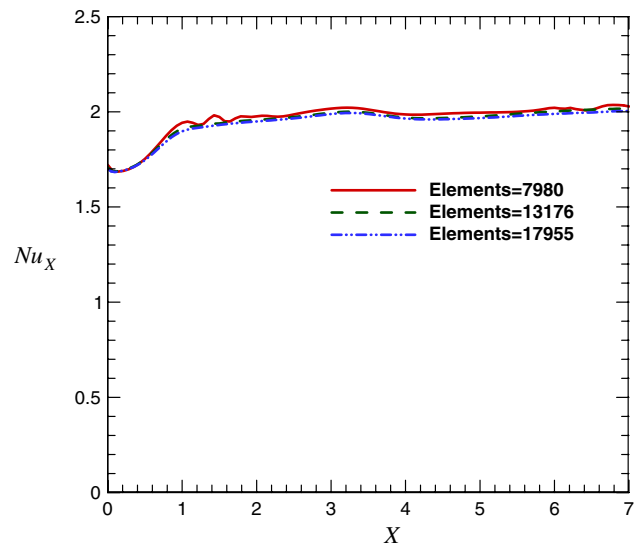| Re	$\frac{Gr}{Re^2}$	L_c	F_c	V_m	$\overline{Nu_X}$	$\overline{Nu_C}$	$\frac{\overline{Nu}_{c,(n)}}{\overline{Nu}_{X,(n)}}$
200	1	0	0	0	3.482(1)	–	–
200	250	0	0	0	1.379(2)	–	–
500	0.16	0	0	0	5.365(3)	–	–
500	40	0	0	0	1.951(4)	–	–
200	1	0.2	0.5	0.628	–	4.130(1)	1.186 $\left(\frac{\overline{Nu}_{c,(1)}}{\overline{Nu}_{X,(1)}}\right)$
200	250	0.2	0.5	0.628	–	1.413(2)	1.025 $\left(\frac{\overline{Nu}_{c,(2)}}{\overline{Nu}_{X,(2)}}\right)$
500	0.16	0.2	0.5	0.628	–	7.348(3)	1.370 $\left(\frac{\overline{Nu}_{c,(3)}}{\overline{Nu}_{X,(3)}}\right)$
500	40	0.2	0.5	0.628	–	2.430(4)	1.246 $\left(\frac{\overline{Nu}_{c,(4)}}{\overline{Nu}_{X,(4)}}\right)$

Fig. 2 Distributions of local Nusselt numbers with three different elements under $Re = 500$, $Gr/Re^2 = 40$

For satisfying the boundary conditions at the outlet of the channel, the length from the horizontal channel to the outlet of the right channel is around 50 which is determined by numerical tests. In addition, an implicit scheme is employed to deal with the time differential terms of the governing equations. The time step $\Delta\tau = \frac{1}{52F_c}$ is chosen for all cases, i.e. totally 52 time steps are required to achieve one periodic cycle.

The dimensionless stream function Ψ is defined as

$$U = \frac{\partial\Psi}{\partial Y}, \quad V = -\frac{\partial\Psi}{\partial X} \tag{20}$$

For indicating the variations of the flow and thermal fields more clearly, the streamlines and isothermal lines in the vicinity of the horizontal channel are presented only. The sign '↑' in the following figures indicates the moving direction of the horizontal channel's movement.

Figure 3a indicates the distributions of the streamlines of the stationary state for $Re = 200$, $Gr/Re^2 = 1$ situation. The arrow sign '↑' in the figure of streamlines indicates the flow direction of streamlines. Due to the slight dominance of the forced convection, the inlet cooling fluids impinge on the top surface directly and turn to the right. The phenomenon of rebound of the fluid on the top surface is hardly observed, and two apparent circulation zones appear. The distributions of the isothermal lines corresponding to Fig. 3a are shown in Fig. 3b. The distributions of the isothermal lines on the impingement region mentioned above are denser than these of the other regions. Thermal stratification layers could be observed near the top corner of the far right side since the heat surface is on the top position and the forced convection is weak.
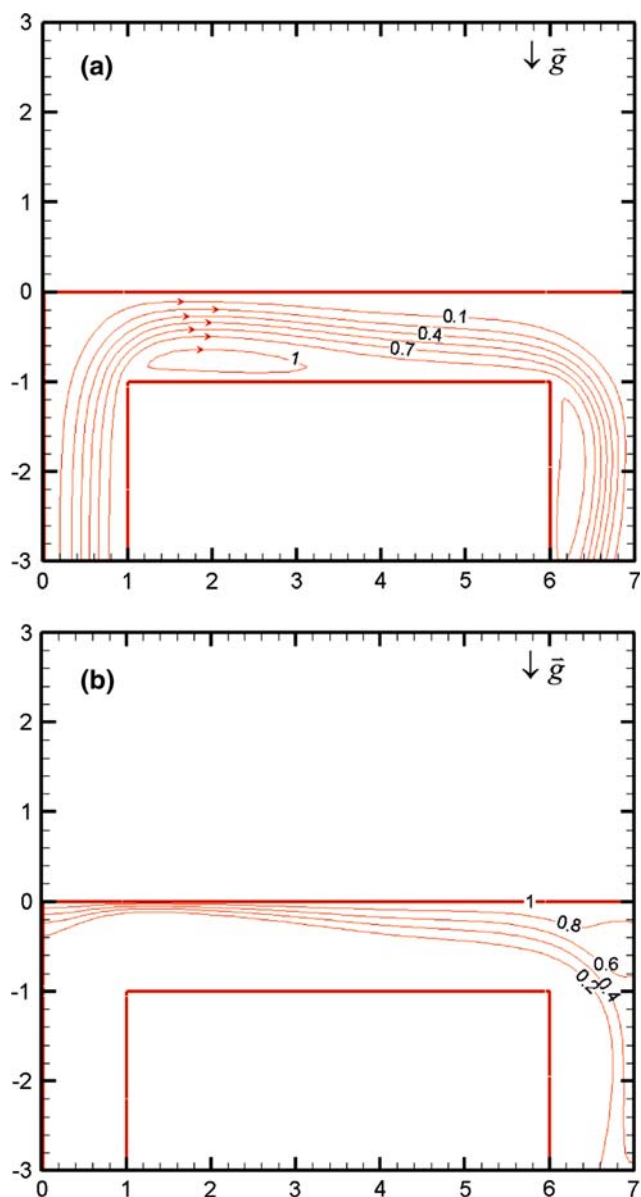
Fig. 3 a The distributions of the streamlines for $Re = 200$, $Gr/Re^2 = 1$. **b** The distributions of the isothermal lines for $Re = 200$, $Gr/Re^2 = 1$
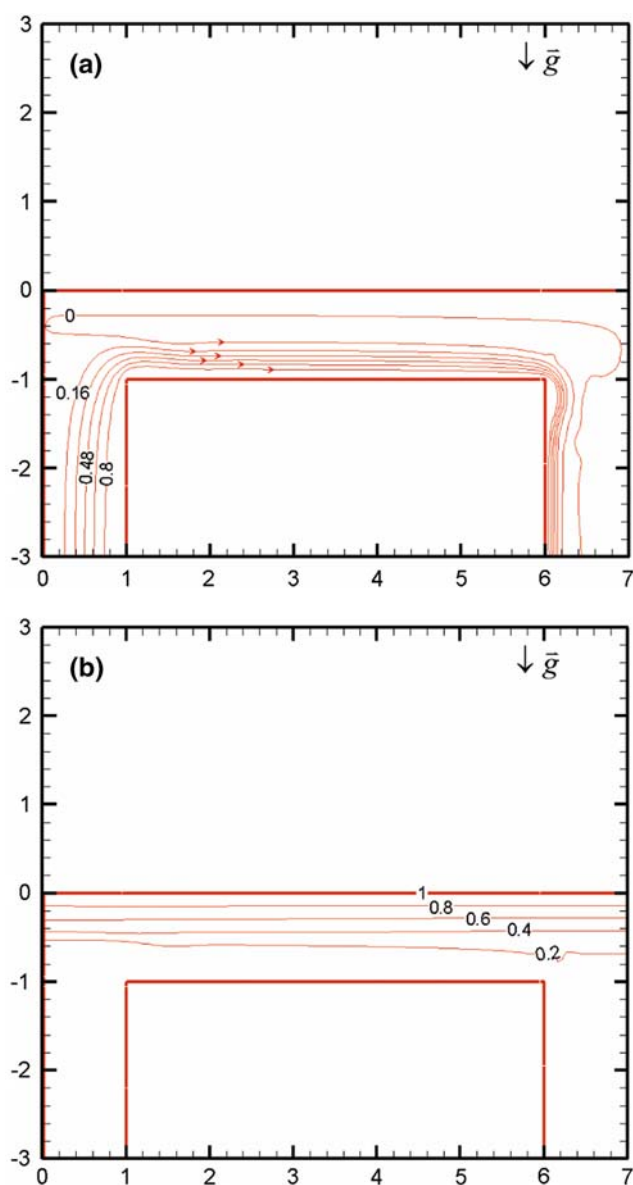
Fig. 4 a The distributions of the streamlines for $Re = 200$, $Gr/Re^2 = 250$. **b** The distributions of the isothermal lines for $Re = 200$, $Gr/Re^2 = 250$

Figure 4a indicates the distributions of streamlines of the stationary state for $Re = 200$, $Gr/Re^2 = 250$ situation. Opposite to the above situation, the natural convection plays a role in this situation. Due to the position of the heat surface, the thermal stratification layers form firmly along the top surface which causes the inlet cooling fluids to be unable to impinge on the top surface directly like the situation mentioned above. Then the inlet cooling fluids flow through the lower region of the horizontal channel, and the circulation zone could not be observed. The distributions of the isothermal lines corresponding to Fig. 4a are shown in Fig. 4b. The influence of the thermal stratification layers is

strong, and the distributions of the isothermal lines are almost uniform along the top heat surface.

Figure 5a and b indicates the distributions of the streamlines and isothermal lines for $Re = 500$, $Gr/Re^2 = 0.16$ situation, respectively. As the Reynolds number increases, the forced convection becomes dominant. Therefore, the variations of both the streamlines and isothermal lines are similar to these shown in Fig. 3a and b.

Figure 6a and b shows the distributions of the streamlines and isothermal lines for $Re = 500$, $Gr/Re^2 = 40$ situation, respectively. The natural convection becomes apparent, then the thermal stratification layers forming
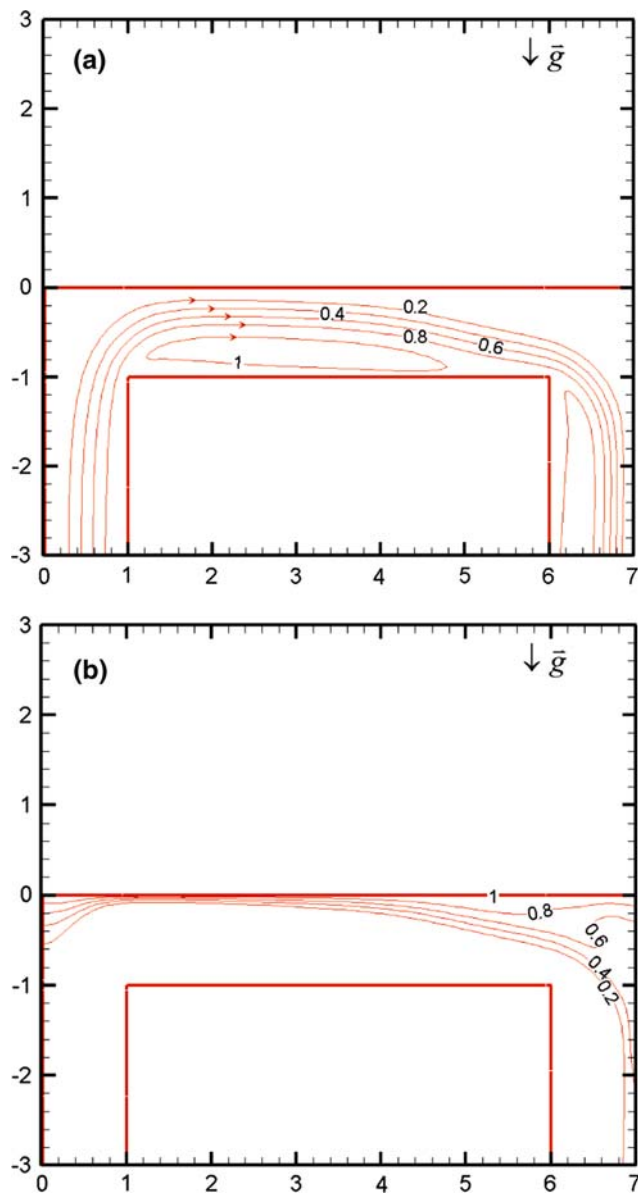
Fig. 5 a The distributions of the streamlines for $Re = 500$, $Gr/Re^2 = 0.16$. **b** The distributions of the isothermal lines for $Re = 500$, $Gr/Re^2 = 0.16$

Fig. 6 a The distributions of the streamlines for $Re = 500$, $Gr/Re^2 = 40$. **b** The distributions of the isothermal lines for $Re = 500$, $Gr/Re^2 = 40$

along the top surface are observed. However, when the Reynolds number increases, a slight impingement on the top surface near the inlet is discovered because of the strong impulse of the cooling fluids. This phenomenon is different from that shown in Fig. 4a. Accompanying with the results shown in Fig. 6a, the distributions of the isothermal lines shown in Fig. 6b near the left side of the top surface are denser than those of the other regions.

The distributions of the local Nusselt number Nu_x on the heat surface of the above four cases are indicated in Fig. 7. As the condition of the dominance of forced convection occurs, the impingement phenomenon could be observed on the left side of the top surface. Therefore, the maximum
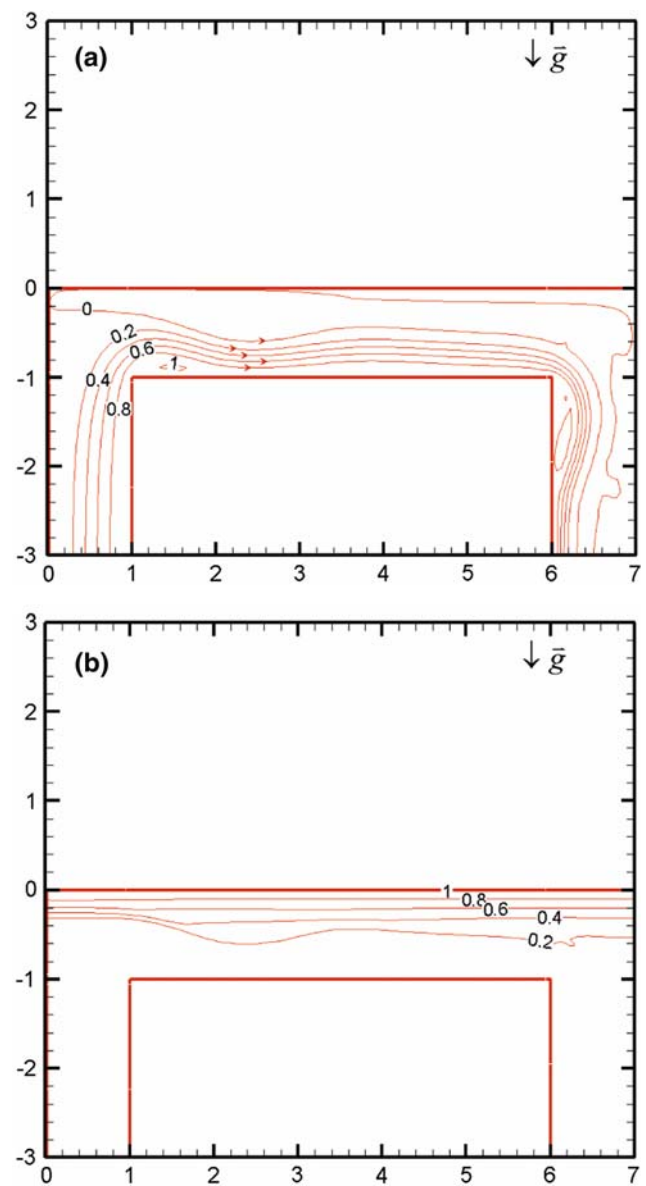
local Nusselt number appears at the corresponding position of the impingement, and the local Nusselt number decreases gradually with the increment of X. Oppositely, as the effect of the natural convection becomes stronger, the thermal stratification layers appear along the top surface which causes the distributions of the local Nusselt number on the top surface to be flat.

Figure 8a indicates the variation of dimensionless mass flow rate $\dot{M}_{exit}$ at the exit ($\overline{HD}$ surface) of the right vertical channel in a cycle time for $Re = 200$, $Gr/Re^2 = 1$, $F_c = 0.2$ and $L_c = 0.5$ situation. As the channel is in the stationary state, the dimensionless mass flow rate at the inlet ($\overline{AE}$ surface) of the left vertical channel $\dot{M}_{inlet}$ is
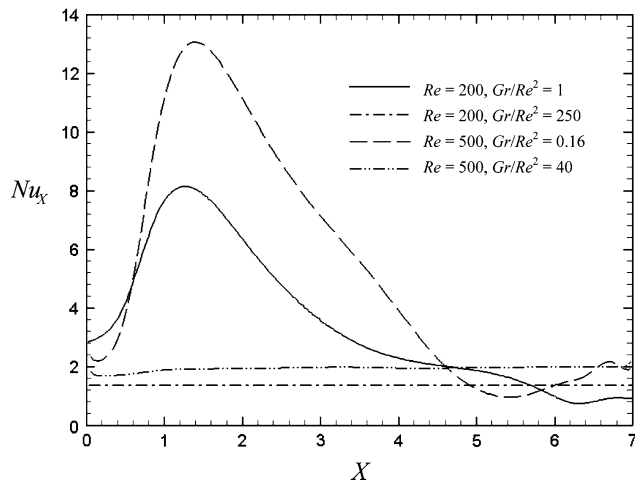
Fig. 7 The distributions of local Nusselt numbers

constant and equal to 1. Due to the conservation of mass, the mass flow rate at the exit of the channel should be constant and equal to 1. However, the reciprocating motion of the channel leads to the volume of the channel to be changed relative to the volume of the channel in the stationary state.

The mass flow rate at the exit of the cooling channel $\dot{M}_{exit}$ could be calculated by the following equation.

$$\dot{M}_{exit} = \dot{M}_{inlet} - 2V_cW \qquad (21)$$

where

$$\dot{M}_{inlet} = \sum V_{n,inlet}\,\Delta W = V_0W \qquad (22)$$

$$\dot{M}_{exit} = \sum V_{n,exit}\,\Delta W \qquad (23)$$

in which $V_{n,exit}$ is the local velocity at the exit of the X axis, ΔW the unit width of the exit.

The magnitude of $2V_cW$ indicates the variation of the dimensionless mass flow rate in the channel corresponding to the variation of the volume of the channel caused by the reciprocating motion. In the former half cycle $\left(\tau = 0 \sim \frac{\tau_p}{2}\right)$, the movement of the channel is from the bottom to top positions, and the volume of the channel is enlarged. In order to supplement the enlarged volume of the channel, the magnitude of $\dot{M}_{exit}$ should be decreased relative to the magnitude of $\dot{M}_{inlet}$. At some stages the magnitudes of $2V_cW$ are possibly larger than the magnitude of $\dot{M}_{inlet}$, and the values of $\dot{M}_{exit}$ become negative which means that some fluids sucked from the surroundings via the exit into the channel. The variations of the vertical velocities on the exit at $\tau = \frac{\tau_p}{4}$ are shown in Fig. 8b. The positive magnitudes of vertical velocities mean the fluids of the surroundings to flow into the channel via the exit. Oppositely, in the latter half cycle $\left(\tau = \frac{\tau_p}{2} \sim \tau_p\right)$, the volume of the channel is contracted and
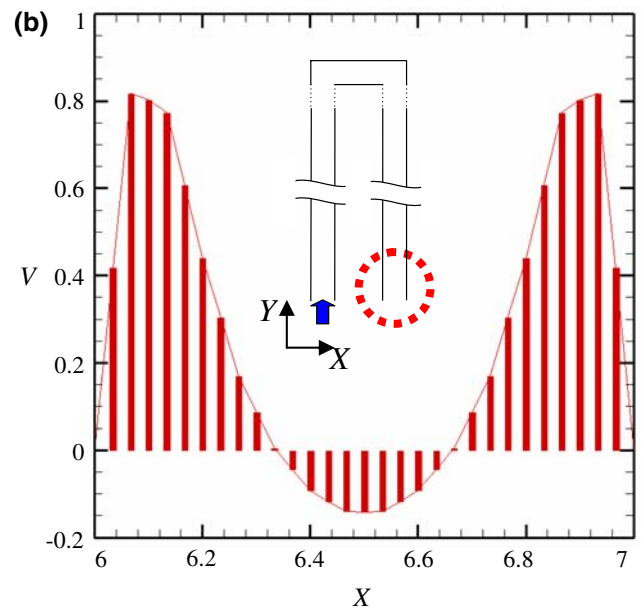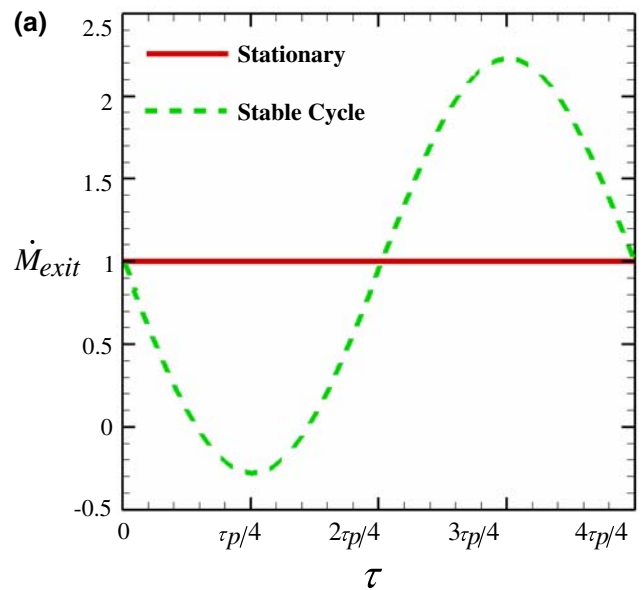

Fig. 8 **a** The variation of dimensionless mass flow rate $\dot{M}_{exit}$ at the exit of the cooling channel in a cycle time for $Re = 200$, $Gr/Re^2 = 1$, $F_c = 0.2$, and $L_c = 0.5$ situation. **b** The vertical velocity profile at the outlet end of the channel at time $\tau_p/4$ for $Re = 200$, $Gr/Re^2 = 1$, $F_c = 0.2$, and $L_c = 0.5$ situation

some fluids in the channel are extraordinarily exhausted to the surroundings via the exit. In these stages, the magnitudes of $\dot{M}_{exit}$ are larger than that of $\dot{M}_{inlet}$.

In this study, the results of the cases of $Re = 200$, $Gr/Re^2 = 1$ and $Re = 500$, $Gr/Re^2 = 0.16$ could be categorized as a flow in which the forced convection is dominant. The variations of streamlines and isothermal lines are similar to those shown in the previous study [15]. The other cases of the dominance of the natural convection flow are indicated exclusively.

Fig. 9 A history of distributions of streamlines of one cycle for $Re = 200$, $Gr/Re^2 = 250$, $F_c = 0.2$, and $L_c = 0.5$ situation
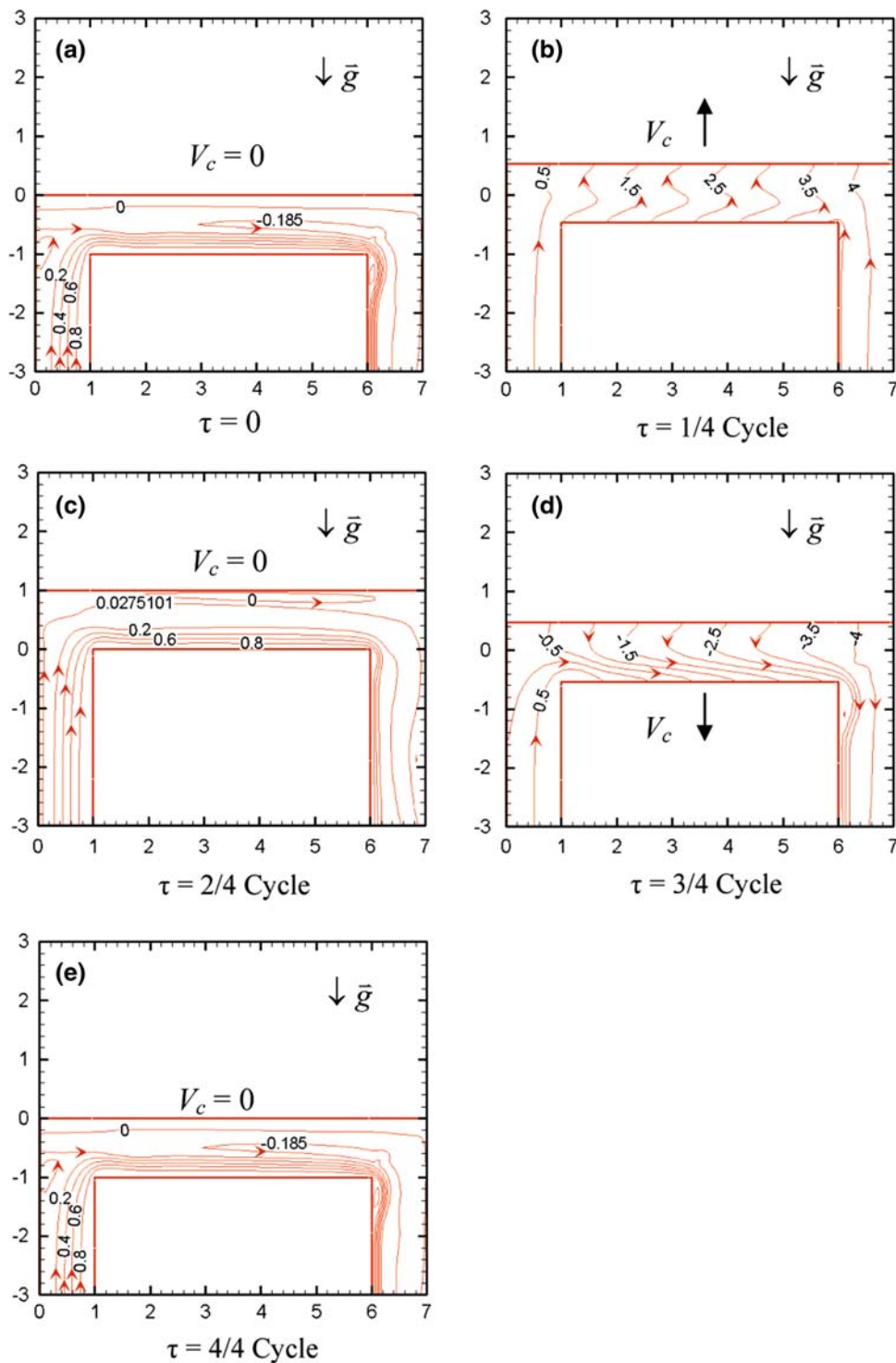

Figure 9 shows a history of distributions of streamlines of one cycle for $Re = 200$, $Gr/Re^2 = 250$, $F_c = 0.2$, and $L_c = 0.5$ situation, respectively. In Fig. 9a, the horizontal channel of which the velocity is zero is at the lowest position. Phenomena are somewhat similar to these of the stationary one shown in Fig. 4. The thermal stratification layers exist on the top surface, and the fluids flow through the low region of the horizontal channel. The streamlines are then observed near the bottom surface only. In Fig. 9b, the horizontal channel has the maximum upward velocity which causes the volume of the channel to be enlarged. As a result, the fluids flow upwards to supplement the enlarged space, accompanying with the results the directions of the streamlines are upward. Figure 9c indicates the reciprocating channel at the

Fig. 10 A history of distributions of isothermal lines of one cycle for $Re = 200$, $Gr/Re^2 = 250$, $F_c = 0.2$, and $L_c = 0.5$ situation
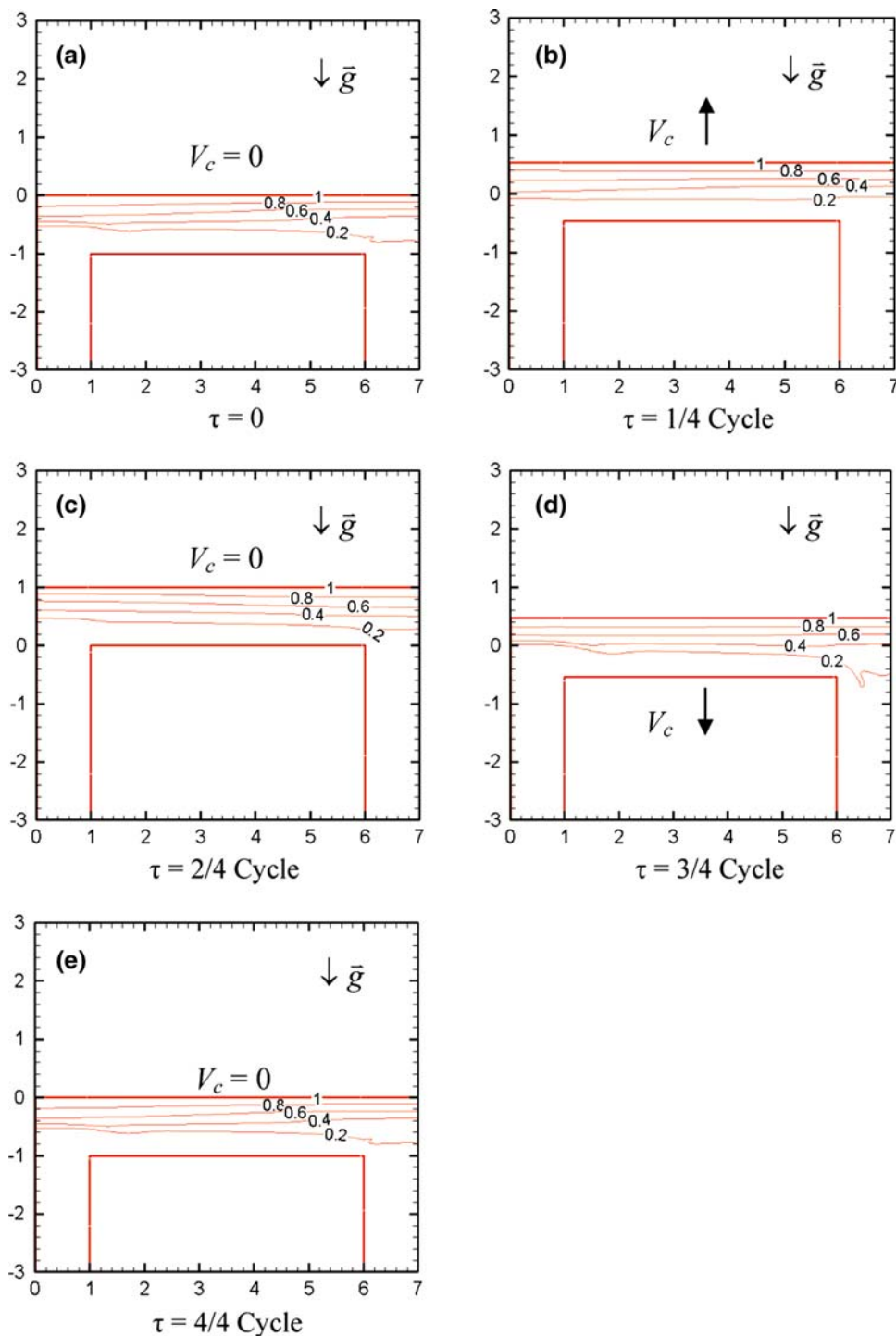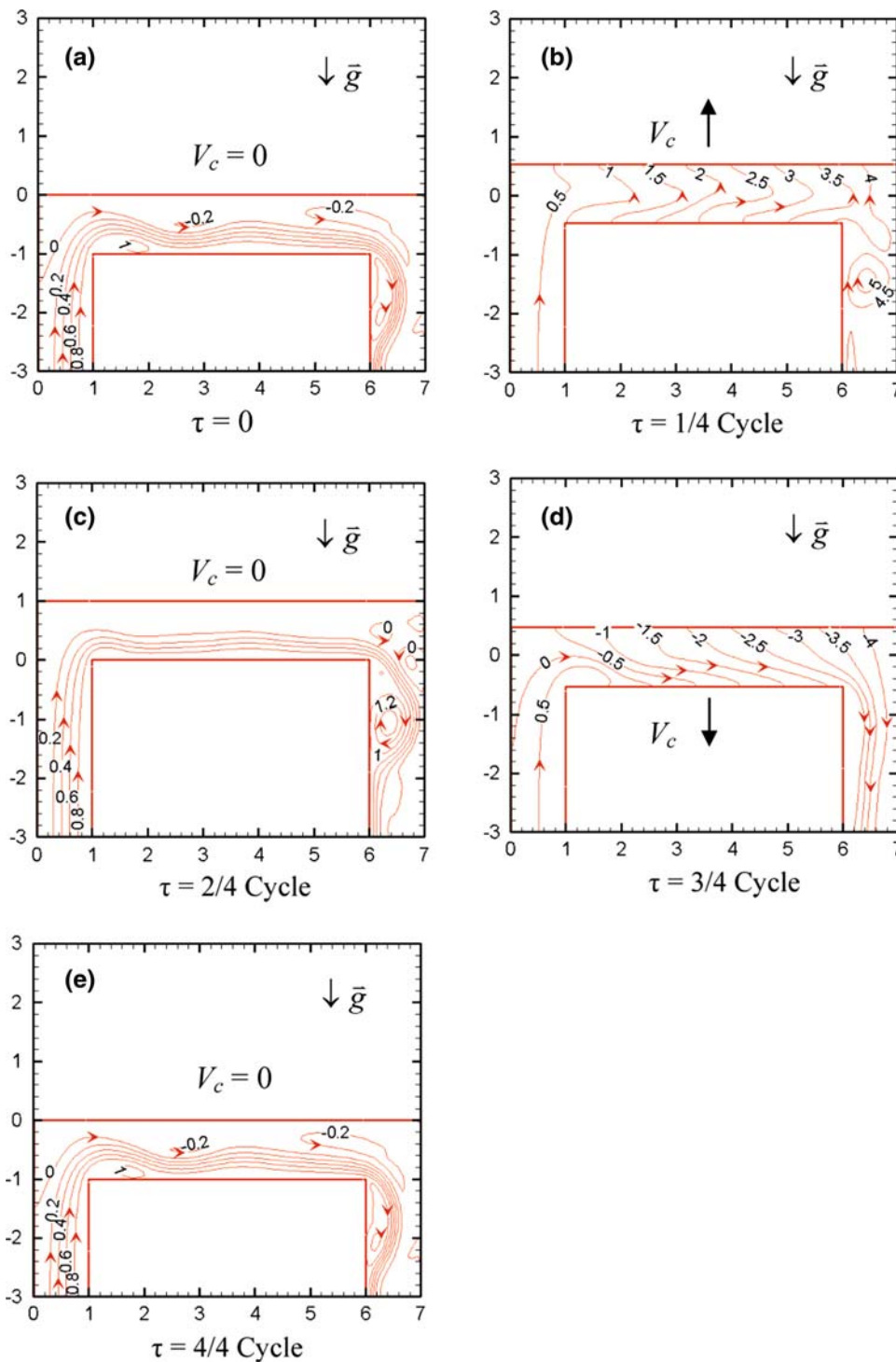
highest position and the velocity is zero. The fluids flow through the low region of the horizontal channel due to the thermal stratification layers occupying the upper region of the horizontal channel. This phenomenon is like that of Fig. 9a situation. Figure 9d shows the horizontal channel to have the maximum downward velocity. The volume of the whole channel is contracted which causes the fluid to be forced to flow quickly to the exit. Then the directions of the

streamlines are from upper region to low right region. Figure 9e is the end of a cycle and the variations of the streamlines equal to these of the onset of a cycle shown in Fig. 9a.

Figure 10a–e indicates a history of distributions of isothermal lines of one cycle which are corresponding to the variations of the streamlines shown in Fig. 9a–e, respectively. Due to the weakness of Reynolds number
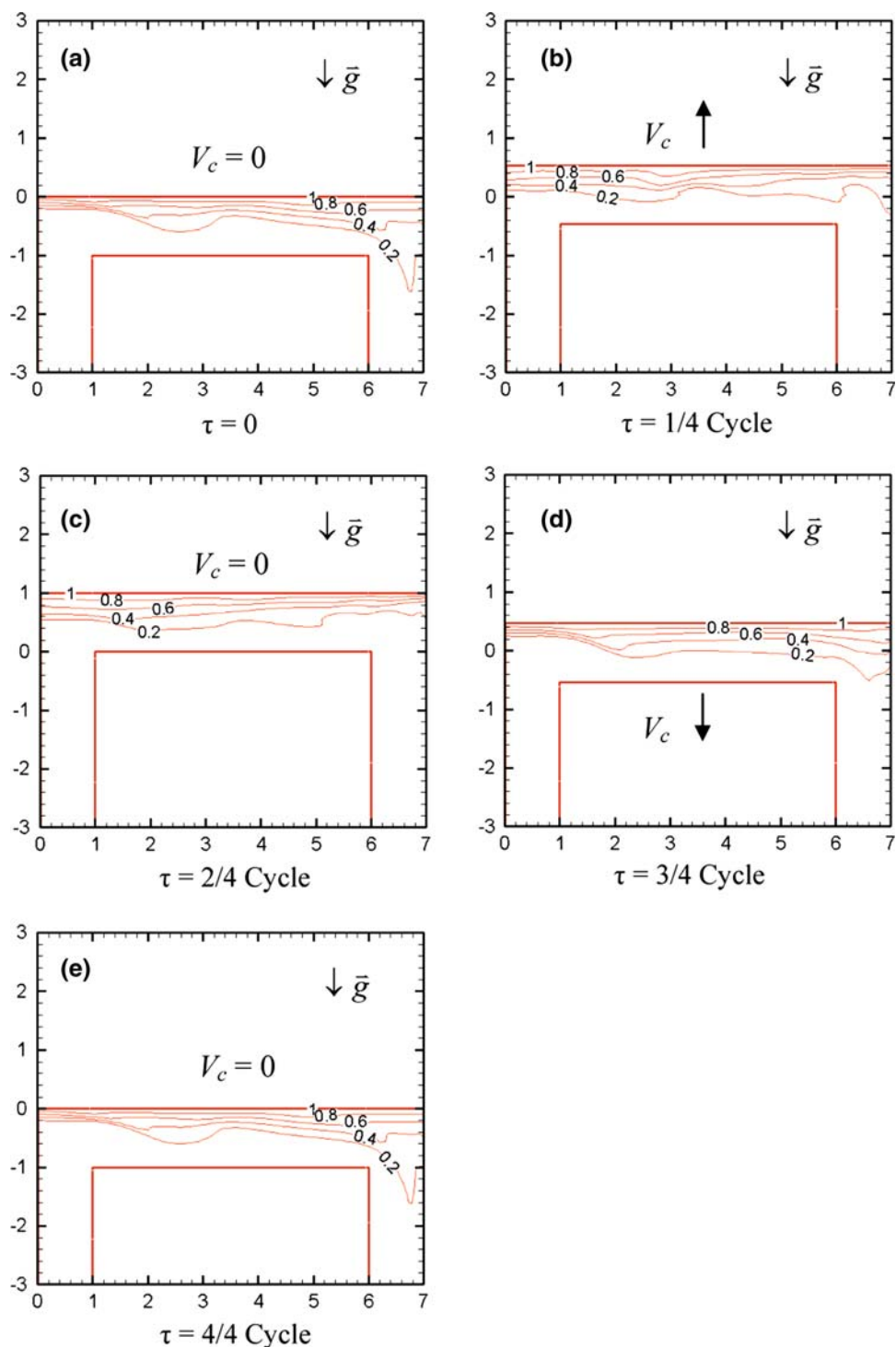
Fig. 11 A history of distributions of streamlines of one cycle for $Re = 500$, $Gr/Re^2 = 40$, $F_c = 0.2$, and $L_c = 0.5$ situation

($Re = 200$) and the top heat surface, the thermal stratification layers apparently form along the top surface. In Fig. 10a, the horizontal channel is at the lowest position and the velocity is zero, which causes the distributions of the isothermal lines to be similar to those shown in Fig. 4b situation. A slight impingement phenomenon is observed on the left side. Shown in Fig. 10b, the upward velocity of the channel is at the maximum condition. The space of the

channel is enlarged and it is difficult for the impingement phenomenon to occur which causes the distributions of the isothermal lines to be flat in most of the horizontal channel. Afterward, in Fig. 10c the horizontal channel stops at the highest position and the velocity is zero which results in the fluids filling up the horizontal channel promptly. As shown in Fig. 10d, the velocity of the horizontal channel is downward and has the maximum magnitude. Relatively,

Fig. 12 A history of distributions of isothermal lines of one cycle for $Re = 500$, $Gr/Re^2 = 40$, $F_c = 0.2$, and $L_c = 0.5$ situation

the space of the channel is contracted and the fluids are accelerated to flow out of the channel which leads the occupation of the distributions of the isothermal lines in the horizontal channel also to be contracted. Due to the opposite direction of the velocities of the inlet fluids and the channel, the impingement region on the left side of the horizontal channel becomes more apparent than those of

the other figures. In Fig. 10e, the situation proceeds to the end of the cycle; the phenomenon is the same as Fig. 10a.

Figure 11a–e indicates a history of distributions of streamlines of one cycle for $Re = 500$, $Gr/Re^2 = 40$, $F_c = 0.2$, and $L_c = 0.5$ situation. In Fig. 11a, the horizontal channel of which the velocity V_c is zero, stops at the lowest position. The Reynolds number is larger than the

former one shown in Fig. 9, and the larger Reynolds number causes the phenomena of the impingement on the left side and rebound on the right side of the horizontal channel to be more apparent than those in Fig. 9a in spite of the dominance of natural convection ($Gr/Re^2 = 40$). But the thermal stratification layers still exist along the top heat surface of the horizontal channel, and a circulation zone forms along the top surface.

The variations of the streamlines of the horizontal channel at the maximum upward velocity condition are shown in Fig. 11b. Due to the augmentation effect of the space of the channel and the flow direction from the left to right, the directions of the streamlines are then changed to the upward and right directions. In Fig. 11c, the channel stops at the highest position and gets rid of upward effect. The directions of the streamlines from the left to right sides reappear, and a circulation region which is different from that of Fig. 11a does not form along the top surface. In Fig. 11d, the channel has the maximum downward velocity, which causes the directions of the streamlines to be changed from the upper to lower sides uniformly. The end of the cycle is shown in Fig. 11e, and the phenomena indicated in Fig. 11a appear repeatedly.

The distributions of the isothermal lines corresponding to the distributions of the streamlines as shown in Fig. 11a–e are indicated in Fig. 12a–e, respectively. In Fig. 12a, the channel stops at the lowest position. The Reynolds number is 500 and larger than the former one ($Re = 200$) shown in Fig. 10. Then the appearance of the denser distribution of the isothermal lines on the left side of the horizontal channel is obvious, and the phenomenon of rebound mentioned in Fig. 11a is observed. The distributions of the isothermal lines become wavy and are not similar to the former situation shown in Fig. 10a. In Fig. 12b, the velocity of the channel is upward and the space of the channel is enlarged, which neutralizes the effect of impingement caused by the cooling fluids from the left vertical channel. Therefore, the denser distribution of the isothermal lines on the left side of the horizontal channel is hard to be observed. Oppositely, the thermal stratification layers form firmly along the top surface, and the distributions of the isothermal lines become flat slightly. Shown in Fig. 12c, the horizontal channel just stops, and the effect of the augmentation of the space is deleted. The effect of the impingement of the cooling fluid on the distributions of the isothermal lines starts to display again. In Fig. 12d, the horizontal channel has the maximum downward velocity. The space of the whole channel is contracted which causes the effect of the impingement of the cooling fluid on the distributions of the isothermal lines to become more drastic. The denser distribution of the isothermal lines on the left side of the horizontal channel is observed remarkably.
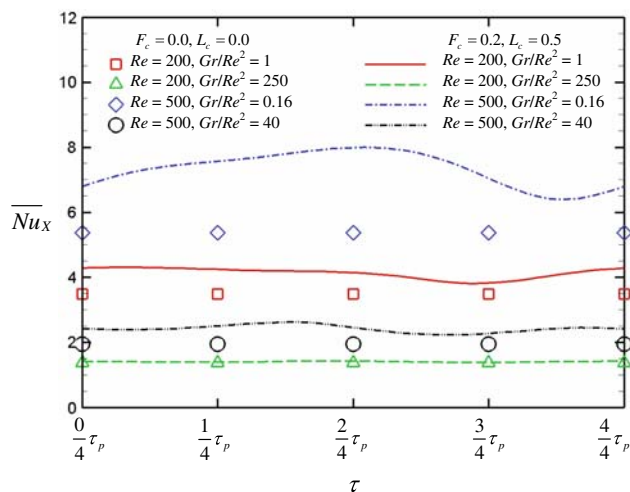

Fig. 13 The distributions of the average Nusselt numbers

Finally, the cycle ends in Fig. 12e which is the same as that shown in Fig. 12a.

Figure 13 indicates the average Nusselt numbers of the stationary and periodical conditions of four different combinations of Re and Gr/Re^2. The definition of average Nusselt number at the stationary state is shown as follows.

$$\overline{Nu_X} = \frac{1}{w_0} \int_{\overline{BC}} Nu_X \, dX$$

$$(F_c = 0, \quad L_c = 0) \tag{24}$$

Because of the existence of the thermal stratification layers induced by the natural convection, the differences of the average Nusselt numbers among the periodical times are slight in the dominance of natural convection situations of $Re = 200$, $Gr/Re^2 = 250$ and $Re = 500$, $Gr/Re^2 = 40$. Oppositely, as the forced convection is dominant ($Re = 500$, $Gr/Re^2 = 0.16$), the influence of the thermal stratification layers becomes weak and the effect of reciprocating motion on the average Nusselt number is apparent. The variations of the average Nusselt numbers form a wavy shape. Based on the results, in most situations, the heat transfer enhancement is achieved by usage of the reciprocating motion.

5 Conclusions

A mixed convection in a Π shape channel affected by a reciprocating motion is performed numerically. The parameters of Reynolds number, Grashof number, frequency and amplitude are considered and the useful results are obtained. Some conclusions could be summarized as follows:

(1) As the natural convection is dominant, the thermal stratification layers form firmly along the top heat surface which causes the distributions of local Nusselt number on the top heat surface to be flat.

(2) As the forced convection plays a role, the impingement phenomenon is close to the inlet region which leads the distributions of local Nusselt numbers to be like a shape of mountain. The summit of the mountain is corresponding to the impingement region.

(3) Generally, the heat transfer enhancement is achieved by usage of the reciprocating motion in this study range.

References

1. Chang SW, Su LM (1999) Heat transfer in a reciprocating duct fitted with transverse ribs. Exp Heat Transf 12:95–115

2. Grassmann PP, Tuma M (1979) Applications of the electrolytic method-II. Mass transfer within a tube for steady, oscillating and pulsating flows. Int J Heat Mass Transf 22:799–804

3. Patera AT, Mikic BB (1986) Exploiting hydrodynamic instabilities resonant heat transfer enhancement. Int J Heat Mass Transf 29(8):1127–1138

4. Kim SY, Kang BH, Hyun AE (1993) Heat transfer in the thermally developing region of a pulsating channel flow. Int J Heat Mass Transf 36(17):1257–1266

5. Nishimura T, Kojima N (1995) Mass transfer enhancement in a symmetric sinusoidal wavy-walled channel for pulsatile flow. Int J Heat Mass Transf 38(9):1719–1731

6. Nishimura T, Taurmoto A, Kawamura Y (1987) Flow and mass transfer characteristics in wavy channels for oscillatory flow. Int J Heat Mass Transf 38:1007–1015

7. Nishimura T, Arakawa S, Murakami D, Kawamura Y (1991) Oscillatory flow in a symmetric sinusoidal wavy-walled channel at intermediate Strouhal numbers. Chem Eng Sci 46:757–771

8. Nishimura T, Arakawa S, Murakami D, Kawamura Y (1989) Oscillatory viscous flow in symmetric sinusoidal wavy-walled channels. Chem Eng Sci 44:2137–2148

9. Chiu CP, Kuo YS (1995) Study of turbulent heat transfer in reciprocating engine using as algebraic grid generation technique. Numer Heat Transf Part A 27:255–271

10. Chang SW, Su LM (1997) Influence of reciprocating motion on heat transfer inside a ribbed duct with application to piston cooling in marine diesel engines. J Ship Res 41(4):332–339

11. Cheng CH, Hung CK (2000) Numerical predictions of flow thermal fields in a reciprocating piston–cylinder assembly. Numer Heat Transf Part A 38:397–421

12. Sert C, Beskok A (2002) Oscillatory flow forced convection in micro heat spreaders. Numer Heat Transf Part A 42:685–705

13. Khaled ARA, Vafai K (2003) Heat transfer and hydromagnetic control of flow exit conditions inside oscillatory squeezed thin films. Numer Heat Transf Part A 43:239–258

14. Chang SW, Su LM, Morris WD, Liou TM (2003) Heat transfer in a smooth-walled reciprocating anti-gravity open thermosyphon. Int J Heat Mass Transf 42:1089–1103

15. Fu WS, Lian SH, Liao YH (2006) An investigation of heat transfer of a reciprocating piston. Int J Heat Mass Transf 49:4360–4371

16. Reddy JN, Gartling DK (1994) In: The finite element method in heat transfer and fluid dynamics, CRC Press, Ann Arbor, pp 47–51